

**State-to-state reactive differential cross sections for the $\text{H} + \text{H}_2$
 $\rightarrow \text{H}_2 + \text{H}$ reaction on five different potential energy surfaces
employing a new quantum wavepacket computer code:
DiffRealWave.**

Marlies Hankel* and Sean C. Smith[†]

*Centre for Computational Molecular Science,
The University of Queensland, QLD 4072, Australia*

Robert J. Allan[‡]

*Advanced Research Computing Group, Daresbury Laboratory,
Daresbury, Warrington, WA4 4AD, UK.*

Stephen K. Gray[§]

Chemistry Division, Argonne National Laboratory, Argonne, Illinois 60439

Gabriel G. Balint-Kurti[¶]

School of Chemistry, University of Bristol, Bristol BS8 1TS, UK

Abstract

State-to-state differential cross sections have been calculated for the hydrogen exchange reaction, $\text{H} + \text{H}_2 \rightarrow \text{H}_2 + \text{H}$, using five different high quality potential energy surfaces with the objective of examining the sensitivity of these detailed cross sections to the underlying potential energy surfaces. The calculations were performed using a new parallel computer code, DiffRealWave. The code is based on the real wavepacket approach of Gray and Balint-Kurti. The calculations are parallelised over the helicity quantum number, Ω' , (i.e. the quantum number for the body-fixed z component of the total angular momentum) and wavepackets for each J, Ω' set are assigned to different processors, similar in spirit to the Coriolis-coupled processors approach of Goldfield and Gray. Calculations for $J = 0 - 24$ have been performed to obtain converged state-to-state differential cross sections in the energy range from 0.4 eV to 1.2 eV. The calculations employ five different potential energy surfaces, the BKMP2 surface and a hierarchical family of four new *ab initio* surfaces (S. L. Mielke, B. C. Garrett, and K. A. Peterson, J. Chem. Phys. **116**, 4142 (2002)). This family of four surfaces has been calculated using 3 different hierarchical sets of basis functions and also an extrapolation to the complete basis set limit, the so called CCI surface. The CCI surface is the most accurate surface for the H_3 system reported to date. Our calculations of differential cross sections are the first to be reported for the A2, A3, A4 and CCI surfaces. They show that there are some small differences in the cross sections obtained from the five different surfaces, particularly at higher energies. The calculations also show that the BKMP2 performs well and gives cross sections in very good agreement with the results from the CCI surface, displaying only small divergences at higher energies.

I. INTRODUCTION

The $\text{H} + \text{H}_2$ exchange reaction and its isotopomers has been the focus of numerous experimental^{1–13} and theoretical^{14–25} studies. It is also the benchmark reaction for the development of new theoretical methods. Aoiz and co-workers recently reviewed the progress in the study of the dynamics of this reaction.²⁶ With advances in experimental^{27,28} and theoretical²⁹ methods very good agreement between theory and experiment has been achieved and only a few issues remain unresolved.²⁶

Several global analytic potential energy surfaces (PES) are available, the LSTH surface,^{30,31} the DMBE surface³² and the BKMP³³ and BKMP2³⁴ surfaces. While these four surfaces are all based on the same initial *ab initio* data different sets of additional data have been used for each surface. Wu *et al.*³⁵ introduced a new surface based on spline fits of exact quantum Monte Carlo (EQMC) calculations. The five surfaces have been used in numerous theoretical studies of the H_3 system. Accurate quantum calculations employing the BKMP2 surface produced results in very good agreement with experiment.²⁶

Four years ago Mielke and co-workers³⁶ calculated a set of three potential energy surfaces for the $\text{H} + \text{H}_2$ exchange reaction using a hierarchical family of basis sets. These were then used to estimate the complete basis set limit of the calculations, thus generating a fourth surface, labelled the CCI surface. These *ab initio* calculations are of nearly full configuration interaction quality and were performed at a set of 4067 nuclear configurations using the aug-cc-pVDZ, aug-cc-pVTZ and aug-cc-pVQZ basis sets. The fitted surfaces are called A2, A3 and A4 respectively. The surfaces were all fitted very accurately to an analytic form. To the best of our knowledge no exact quantum calculations of cross sections have been reported to date employing these four surfaces.

Several theoretical methods for computing state-to-state differential reactive cross sections have been described and applied in the literature. These include the ABC code of Manolopoulos *et al.*³⁷, the code of Launay *et al.*³⁸ and the wavepacket codes of Althorpe *et al.*³⁹ and of Dong Hui Zhang *et al.*⁴⁰ In this paper we report the first calculations of state-to-state differential reactive cross sections based on the real wavepacket approach of Gray and Balint-Kurti.⁴¹ The distinguishing aspects of the theory needed for these calculations are described in the following section (section II). The computer code, DiffRealWave, is currently available under license upon application to the authors.⁴²

Section III is divided into two subsections. The first compares calculations performed with the DiffRealWave with calculations using the ABC³⁷ code to establish the reliability of the new code, while the second subsection reports a comparison of the differential and total cross sections computed using the five different potential energy surfaces investigated in this work. The final section (section IV) presents the conclusions of the paper.

II. THEORY

The real wavepacket method and the theory underlying it has been fully described in a previous publication.⁴¹ There have been many applications of the methodology both by the present authors^{43–48} and by others.^{49–51} All these calculations have either been performed only for total angular momentum $J = 0$ or have been simplified through the use of the helicity decoupling approximation when $J > 0$. For the calculation of state-to-state reactive differential cross sections it is essential to include the full Coriolis coupling terms in the Hamiltonian operator and to treat them accurately.

The real part of the wavepacket is expanded in the form:

$$\Phi^{JM}(\vec{R}, \vec{r}, t) = \sum_{\Omega'} q^{J\Omega'}(R, r, \gamma, t) \frac{1}{Rr} D_{\Omega', M}^J(\omega) \quad (1)$$

where

J = total angular momentum quantum number

M = space-fixed z component of \vec{J}

Ω' = body-fixed z component of \vec{J}

$D_{\Omega', M}^J(\omega)$ = Wigner D Matrix^{52,53}

ω = Euler angles relating the space-fixed and
body-fixed coordinate systems^{52,53}

\vec{R} = (R_x, R_y, R_z)

\vec{r} = (r_x, r_y, r_z) with components measured
relative to the space-fixed axes

$q^{J\Omega'}(R, r, \gamma, t)$ is the component of the body-fixed wavepacket corresponding to J and Ω' . The wavepacket is expressed using body-fixed Jacobi coordinates (R, r, γ) .⁵⁴ The action of the Hamiltonian operator on the wavepacket is given by⁵⁵

$$\hat{H} q^{J\Omega'}(R, r, \gamma, t) =$$

$$\begin{aligned}
& \left\{ -\frac{1}{2\mu_R} \frac{\partial^2}{\partial R^2} - \frac{1}{2\mu_r} \frac{\partial^2}{\partial r^2} \right\} q^{J\Omega'}(R, r, \gamma, t) \\
& - \left(\frac{1}{2\mu_R R^2} + \frac{1}{2\mu_r r^2} \right) \left\{ \frac{1}{\sin \gamma} \frac{\partial}{\partial \gamma} \sin \gamma \frac{\partial}{\partial \gamma} - \frac{\Omega'^2}{\sin^2 \gamma} \right\} q^{J\Omega'}(R, r, \gamma, t) \\
& + V(R, r, \gamma) q^{J\Omega'}(R, r, \gamma, t) + \left(\frac{1}{2\mu_R R^2} \right) (J(J+1) - 2\Omega'^2) q^{J\Omega'}(R, r, \gamma, t) \\
& - \frac{C_{J\Omega'}^+}{2\mu_R R^2} \left\{ \frac{\partial}{\partial \gamma} - \Omega' \cot \gamma \right\} q^{J, \Omega'+1}(R, r, \gamma, t) \\
& - \frac{C_{J\Omega'}^-}{2\mu_R R^2} \left\{ -\frac{\partial}{\partial \gamma} - \Omega' \cot \gamma \right\} q^{J, \Omega'-1}(R, r, \gamma, t)
\end{aligned} \tag{2}$$

where

$$C_{J\Omega'}^\pm = [J(J+1) - \Omega'(\Omega' \pm 1)]^{1/2}. \tag{3}$$

J is a good quantum number and calculations can be carried out separately for each value of J . Ω' is the quantum number for the projection of the total angular momentum onto the body-fixed z -axis. This is not a good quantum number in the sense that the Hamiltonian operator contains centrifugal coupling terms, the last two terms in Eq. (2), which lead to the mixing of wavepackets, $q^{J, \Omega'}(R, r, \gamma, t)$, with different Ω' quantum numbers. In order to compute observables such as reactive cross sections the dynamics have to be solved for many J values. For each J , and for a given parity, either $J+1$ or J (depending on the parity) coupled wavepackets have to be propagated.^{56–60}

Time-dependent methods such as the real wavepacket approach employed here are easily parallelised over Ω' which makes calculations for higher values of J feasible. The coupling matrix is tridiagonal and the wavepacket for Ω' is only coupled to the wavepackets with $\Omega' + 1$ and $\Omega' - 1$. In the parallel version of our wavepacket code each Ω' is assigned to a different processor, similar in spirit to the Coriolis-coupled processors approach of Goldfield and Gray.⁶¹ Each calculation for a set of (J, Ω') can therefore be carried out on a different processor and only neighbouring processors need to communicate with each other.

The wavepacket is now expanded in a basis set of associated Legendre polynomials, $P_{j'\Omega'}(\cos \gamma)$, with $\Omega' \leq \min\{j', J\}$,

$$q^{J\Omega'}(R, r, \gamma, t) = \sum_{j'} \phi^{Jj'\Omega'}(R, r, t) P_{j'\Omega'}(\cos \gamma). \tag{4}$$

Using this basis set the second term and the last two terms of the Hamiltonian have the form

$$\begin{aligned}
2^{\text{nd}} \text{ term} : & \quad \sum_{j'} \left(\frac{1}{2\mu_R R^2} + \frac{1}{2\mu_r r^2} \right) (j'(j' + 1)) \phi^{Jj'\Omega'}(R, r, t) P_{j'\Omega'}(\cos \gamma) \\
5^{\text{th}} \text{ term} : & \quad - \sum_{j'} \frac{C_{J\Omega'}^+ C_{j\Omega'}^+}{2\mu_R R^2} \phi^{Jj',\Omega'+1}(R, r, t) P_{j'\Omega'+1}(\cos \gamma) \\
6^{\text{th}} \text{ term} : & \quad - \sum_{j'} \frac{C_{J\Omega'}^- C_{j\Omega'}^-}{2\mu_R R^2} \phi^{Jj',\Omega'-1}(R, r, t) P_{j'\Omega'-1}(\cos \gamma)
\end{aligned} \tag{5}$$

Leforestier⁶² and Corey and Lemoine⁶³ have developed methods, derived from the generalised DVR method of Light *et al.*,⁶⁴ that use the same γ grid for the different Ω' components of the wavepacket. The grid points are taken to be the associated Gauss-Legendre quadrature points for the case $\Omega' = 0$. For each Ω' value there is a different transformation matrix to transform the wavepacket from the grid representation to the basis set representation and back (see Ref. 55 and references therein for more details).

This becomes important when the action of the last two terms of the Hamiltonian operator has to be evaluated. For the evaluation of these two terms the wavepacket for $\Omega' - 1$ and the wavepacket for $\Omega' + 1$ have to be known. These have to be passed from the two processors on which the calculations for the $(J, \Omega' - 1)$ and $(J, \Omega' + 1)$ combination are done to the processor that carries out the calculation for (J, Ω') . To evaluate the action of the Hamiltonian operator on the wavepacket these two wavepackets (i.e. for $J, \Omega' - 1$ and $J, \Omega' + 1$) have to be transformed from the grid representation to the basis set representation. Both transformation matrices, for $\Omega' - 1$ and $\Omega' + 1$, are different to the transformation matrix used on the processor for Ω' . Therefore these two transformation matrices also have to be calculated on each processor.

The details of using the inversion symmetry or the parity quantum number, are not discussed here. The use of parity involves taking plus and minus combinations of the wavepacket components for positive and negative values of the helicity quantum number Ω . The reader is referred to past papers for a detailed discussion of the use of parity.^{55,56,65} In the present work the initial rotational state of the diatomic is taken to be $j = 0$. The initial parity is therefore always equal to $(-1)^J$ and for every J value there is only one parity. In general (for $j \neq 0$) both parities will contribute to the cross sections.

A. Limiting the Coriolis coupling potential in the presence of a deep well

The real wavepacket approach^{41,66} has been used in the present work. This approach requires that the spectrum of the Hamiltonian operator (i.e. the range of energies encompassed by the grid or basis functions) is scaled and shifted, such that it lies between -1 and 1 . To ensure the efficiency of the calculations it is important that the spectrum of \hat{H} should be limited to the smallest possible range commensurate with an accurate computation of the dynamics. In order to achieve this a cut-off or maximum value, V_{\max} , is imposed on the potential. The various terms in the Hamiltonian arising from the angular part of the kinetic energy operator contain factors of $1/R^2$ and $1/r^2$ (see Eqs. (2) and (5)). The energy associated with these terms must be limited in the same way as that arising from the potential. The centrifugal coupling terms, Eq. (5), pose a particular problem as at small values of R and r , where they become unphysically large, the off-diagonal Coriolis terms (the last two terms in the Hamiltonian operator) would cause the spectrum of \hat{H} to diverge. Serious problems arise if we simply impose a cut-off on these non-diagonal terms. We therefore use an effective potential, the potential and these terms, to limit the spectrum of the Hamiltonian operator.

The minimum value of the effective potential for a given value of J , j' and Ω' , and for a fixed value of R , is given by:

$$V_{\text{eff,min}}^{Jj'\Omega'}(R) = V_{\min}(R) + V_{\text{diag}}^{Jj'\Omega'}(R) \quad (6)$$

where

$$V_{\text{diag}}^{Jj'\Omega'}(R) = \left(\frac{1}{2\mu_R R^2} \right) (J(J+1) + j'(j'+1) - 2(\Omega')^2) \quad (7)$$

and $V_{\min}(R)$ is the lowest value of the potential for a fixed value of R . If $V_{\text{eff,min}}^{Jj'\Omega'}(R)$ is greater than V_{\max} then $V_{\text{diag}}^{Jj'\Omega'}(R)$ is set equal to $(V_{\max} - V_{\min}(R))$. This ensures that the potential plus the diagonal centrifugal term is only cut off when their sum is greater than V_{\max} . This procedure is important if the potential features a minimum or a deep well. If the diagonal term is cut-off for a pair (j', Ω') then the two off-diagonal terms $C_{J\Omega'}^+ C_{j'\Omega'}^+ / (2\mu_R R^2)$ and $C_{J\Omega'}^- C_{j'\Omega'}^- / (2\mu_R R^2)$ are set to zero for this pair of rotational and helicity quantum number. For the term $V_{\text{diag}}^{Jj'}(r) = j'(j'+1)/2\mu_r r^2$ we also first calculate the minimum of the potential for fixed r and then proceed in an analogous manner as for the effective potential in the R

coordinate. Care is also taken to keep track of the actual maximum value of the effective potentials used so as to use the correct spectral range of the Hamiltonian in calculating the required energy scaling.

B. The initial wavepacket

For a reaction $A+BC \rightarrow AB+C$ the initial wavepacket is set up on a grid in reactant Jacobi coordinates where R^a represents the scattering coordinate (distance from the atom A to the molecule BC), r^a , the internal coordinate and γ^a the Jacobi angle. The corresponding product Jacobi coordinates are denoted as (R^c, r^c, γ^c) . The wavepacket propagation is started in the asymptotic region of the reactant channel at a scattering distance $R^a = R_0$ and the initial wavepacket is centred around R_0 . The wavepacket also needs to be given a momentum in the direction of the interaction region. The time-dependent wavepacket propagation is an initial value problem, starting from one initial vibrational rotational state of the reactant molecule $\varphi_{v,j}^{BC}(r^a, \gamma^a) = \phi_{v,j}(r^a)P_j(\cos \gamma^a)$, where $\phi_{v,j}(r^a)$ represents the vibrational wave function, calculated using a Fourier grid Hamiltonian method, and $P_j(\cos \gamma^a)$ are Legendre polynomials. The initial wavepacket used in all calculations presented in this work is of the form

$$q(R^a, r^a, \gamma^a; t = 0) = w(R^a - R_0) e^{-ik_0(R^a - R_0)} \varphi_{v,j}^{BC}(r^a, \gamma^a). \quad (8)$$

where $w(R^a - R_0)$ is a sinc function $\text{sinc}(\alpha R^a) = \sin(\alpha R^a)/\alpha R^a$, whose use in quantum reactive wavepacket calculations has been discussed elsewhere by some of the present authors.⁶⁷

The analysis of the results of a quantum reactive wavepacket calculation requires the knowledge of the momentum distribution of the initial wavepacket in the asymptotic reactant region. For the exact calculation of total and differential cross sections, where dynamical calculations are needed for all total angular momenta, J , contributing to the cross section, the scattering coordinate of the centre of the initial wavepacket, R_0 , will inevitably be in a region where the centrifugal potential is still significantly different from zero for some values of J . We therefore use the “trick analysis” procedure^{45,56,68} in which we propagate the initial wavepacket backwards in the reactant scattering coordinate so as to ascertain the momentum distribution, $\bar{g}(-k_{v,j})$, of the initial wavepacket in the asymptotic reactant region.

C. Transformation to product Jacobi coordinates

For the analysis of the product quantum states the wavepacket must be expressed in terms of product Jacobi coordinates. In the present work, as in our past calculations,^{43,44} this was accomplished by defining the initial wavepacket in reactant Jacobi coordinates, as described above, and immediately transforming it into product Jacobi coordinates. The (J, Ω') component of the wavepacket in product Jacobi coordinates is given in terms of the initial wavepacket, which is assumed to correspond to a well defined projection of the total angular momentum on the reactant body-fixed z axis, Ω , by the expression:

$$q^{J\Omega'}(R^c, r^c, \gamma^c) = q^{J\Omega}(R^a, r^a, \gamma^a) \frac{R^c r^c}{R^a r^a} d_{\Omega\Omega'}^J(\beta). \quad (9)$$

where $d_{\Omega\Omega'}^J(\beta) = D_{\Omega\Omega'}^J(0\beta 0)$ is a reduced Wigner rotation matrix^{52,53} and β is the angle between the vectors \vec{R}^a and \vec{R}^c .

D. Analysis of wavepacket and calculation of differential cross sections

The analysis of the wavepacket arising from a real wavepacket calculation and the extraction of body-fixed \mathbf{S} matrices and reaction probabilities has been described previously.^{41,56,69} As discussed by Althorpe³⁹ it is important for the calculation of differential cross sections to evaluate the \mathbf{S} matrix initially in a space-fixed reference frame. The reason for this is that the Coriolis coupling terms, which occur in the body-fixed coordinate system, (see Eq. (5)) are very long ranged and prevent the correct evaluation of the \mathbf{S} matrix elements for $J > 0$. In the space-fixed coordinate system this coupling is absent and the (ℓ, j) channels are not subject to any long-range coupling. The first step in the analysis is identical to that used in previous work. The propagation of the wavepacket is achieved by a Chebyshev iteration and at each time step (or iteration step⁴¹) a cut is taken through the wavepacket along an analysis line, $R = R_\infty$, corresponding to a value of the product scattering coordinate in the asymptotic region of the potential. This yields the quantity $q^{J\Omega'}(R = R_\infty, r, \gamma, t)$, which is then expanded in terms of product vibrational-rotational eigenfunctions, $\varphi_{v',j'}(r, \gamma)$, to yield:

$$q^{J\Omega'}(R = R_\infty, r, \gamma, t) = \sum_{v',j'} C_{v,j,\Omega \rightarrow v',j',\Omega'}^J(t) \varphi_{v',j'}(r, \gamma). \quad (10)$$

The time-dependent expansion coefficients may be written as

$$C_{v,j,\Omega \rightarrow v',j',\Omega'}^J(t) = \int \varphi_{v',j'}^*(r, \gamma) q^{J\Omega'}(R = R_\infty, r, \gamma, t) dr d\gamma. \quad (11)$$

In the present case as the initial diatomic is in its $j = 0$ state, the initial $\Omega = 0$. The coefficients in Eq. (11) are then half Fourier transformed to give a set of energy-dependent coefficients $A_{v,j,\Omega \rightarrow v',j',\Omega'}^J(E)$

$$A_{v,j,\Omega \rightarrow v',j',\Omega'}^J(E) = \frac{1}{2\pi} \int_0^\infty e^{iEt/\hbar} C_{v,j,\Omega \rightarrow v',j',\Omega'}^J(t) dt. \quad (12)$$

These energy-dependent coefficients are proportional to the body-fixed scattering **S** matrix elements.^{41,56,69}

In order to allow for the effect of the long range Coriolis coupling in the body-fixed coordinate system we now transform to the space-fixed basis. The transformation from body-fixed to space-fixed basis functions takes the form of a unitary transformation:

$$A_{v,j,\ell \rightarrow v',j',\ell'}^J(E) = \sum_{\Omega' \Omega}^{\min(j',J)} T_{\ell \Omega}^J A_{v,j,\Omega \rightarrow v',j',\Omega'}^J(E) T_{\ell' \Omega'}^J \quad (13)$$

where $T_{\ell' \Omega'}^J$ are the elements of the transformation matrix, **T**^c, and $T_{\ell \Omega}^J$ are the elements of the transformation matrix, **T**^a, for the products and reactants respectively. In our case $\ell = J$ as a consequence of the initial condition $j = 0$. Because of this also $\Omega = 0$ and the second transformation matrix, **T**^a, with elements $T_{\ell \Omega}^J$ for transforming the reactant basis set could be omitted in this case.

The transformation matrix with elements $T_{\ell' \Omega'}^J$, is the matrix which diagonalises the Coriolis coupling matrix (i.e. whose columns are the eigenvector of this matrix). The diagonal elements of the Coriolis coupling matrix are given by Eq. (7) and the off diagonal terms by $-(C_{J\Omega'}^+ C_{j\Omega'}^+)/ (2\mu_R R^2)$. The eigenvalues of the matrix are of the form $(\ell'(\ell' + 1))/ (2\mu_R R^2)$, and we use these known eigenvalues to check for the correctness of the computation of this transformation matrix. The elements of **T**^a are calculated in the same way as for the product basis.

The **S** matrix elements in the space-fixed coordinate system are then given by:⁴¹

$$S_{v,j,\ell \rightarrow v',j',\ell'}^J(E) = -\frac{\hbar^2 a_s}{(1 - E_s^2)^{1/2}} \left(\frac{k_{v'j'} k_{vj}}{\mu_r \mu_p} \right)^{1/2} e^{-ik_{v'j'} R_\infty} \frac{2A_{v,j,\ell \rightarrow v',j',\ell'}^J(E)}{\bar{g}(-k_{vj})} \quad (14)$$

where a_s is the energy scaling factor, E_s is the scaled and shifted energy corresponding to the energy E , μ_r and μ_p are the reduced masses for the scattering coordinates in the reactant and product Jacobi coordinates respectively. $k_{v'j'}$ is the wavevector component associated with the product channel and is calculated as

$$k_{v'j'} = \sqrt{2\mu_p \left(E - \left(\varepsilon_{v'j'} + \frac{\ell'(\ell' + 1)}{2\mu_p R_\infty^2} \right) \right)}. \quad (15)$$

The factor of $(\ell'(\ell' + 1))/(2\mu_p R_\infty^2)$ takes account of the fact that the centrifugal potential differs from zero at the analysis line.

As the centrifugal potential is not zero at the analysis line, the phase of the \mathbf{S} matrix must be adjusted to take proper account of this and of the fact that the analysis is performed at the analysis line which is assumed to be in the asymptotic region of the potential (including the centrifugal potential). These phase adjustments can only be performed in the space-fixed basis set where there are no residual Coriolis coupling terms.

The correction to the phase in the exit channel is:

$$\delta\eta_{v'j'\ell'} = \int_{R_\infty}^{\infty} dR \left\{ \sqrt{2\mu_p \left(E - \varepsilon_{v'j'} - \frac{\ell'(\ell' + 1)}{2\mu_p R^2} \right)} - \sqrt{2\mu_p (E - \varepsilon_{v'j'})} \right\} \quad (16)$$

while in the entrance channel the equivalent correction is:

$$\delta\eta_{vj\ell} = \int_{R_0}^{\infty} dR \left\{ \sqrt{2\mu_r \left(E - \varepsilon_{vj} - \frac{\ell(\ell + 1)}{2\mu_r R^2} \right)} - \sqrt{2\mu_r (E - \varepsilon_{vj})} \right\} \quad (17)$$

where in the present case $v = 0$, $j = 0$ and $\ell = J$.

The integrals in Eqs. (16) and (17) can be performed analytically to yield (see Ref. 70 integrals number 2.265 and 2.266):

$$\begin{aligned} \delta\eta &= \int_{R^*}^{\infty} dR \left\{ \sqrt{a - \frac{b}{R^2}} - \sqrt{a} \right\} \\ &= -\sqrt{a(R^*)^2 - b} + \sqrt{b} \arcsin \left(-\sqrt{\frac{b}{a(R^*)^2}} \right) + \sqrt{a}R^* \end{aligned} \quad (18)$$

where $R^* = R_\infty$ or $R^* = R_0$, $a = 2\mu_p(E - \varepsilon_{v'j'})$ or $a = 2\mu_r(E - \varepsilon_{vj})$ and $b = \ell'(\ell' + 1)$ or $b = \ell(\ell + 1)$ for Eqs. (16) and (17) respectively. The final expression for the \mathbf{S} matrix elements, together with the phase corrections (Eqs. (16) and (17)) is therefore:

$$S_{v,j,\ell \rightarrow v',j',\ell'}^J(E) = -\frac{\hbar^2 a_s}{(1 - E_s^2)^{1/2}} \left(\frac{k_{v'j'} k_{vj}}{\mu_r \mu_p} \right)^{1/2} \frac{2A_{v,j,\ell \rightarrow v',j',\ell'}^J(E)}{\bar{g}(-k_{vj})} e^{-i(k_{v'j'} R_\infty + \delta\eta_{v'j'\ell'} + \delta\eta_{vj\ell})} \quad (19)$$

Having calculated the \mathbf{S} matrix in the space-fixed basis we now transform back to the body-fixed basis using the same transformation matrices, \mathbf{T}^c and \mathbf{T}^a , as before (see Eq. (13) and the comments below it).

$$S_{v,j,\Omega \rightarrow v',j',\Omega'}^J(E) = \sum_{\ell' \ell} T_{\Omega \ell}^J S_{v,j,\ell \rightarrow v',j',\ell'}^J(E) T_{\Omega' \ell'}^J \quad (20)$$

Note that $T_{\Omega' \ell'}^J$ and $T_{\Omega \ell}^J$ are the elements of $(\mathbf{T}^c)^T$ and $(\mathbf{T}^a)^T$. The differential cross section is then given by:^{56,65}

$$\sigma(E, \theta, v, j \rightarrow v', j') = \frac{1}{2j+1} \sum_{\Omega' \Omega} \frac{1}{4 k_{vj}^2} \left| \sum_J (2J+1) S_{v,j,\Omega \rightarrow v',j',\Omega'}^J(E) d_{\Omega \Omega'}^J(\theta) \right|^2. \quad (21)$$

Note, in the present case the initial Ω is fixed to $\Omega = 0$ as part of the initial conditions and therefore the summation over Ω could be omitted.

The integral cross section is obtained from the differential cross section by integration over all angles

$$\sigma(E, v, j \rightarrow v', j') = \int_0^{2\pi} d\phi \int_0^\pi \sin \theta \sigma(E, \theta, v, j \rightarrow v', j') d\theta. \quad (22)$$

The differential cross section does not depend on the angle ϕ and therefore this yields

$$\begin{aligned} \sigma(E, v, j \rightarrow v', j') &= 2\pi \int_0^\pi \sin \theta \sigma(E, \theta, v, j \rightarrow v', j') d\theta \\ &= \frac{\pi}{k_{vj}^2} \frac{1}{2j+1} \sum_{\Omega' \Omega} \sum_J (2J+1) \left| S_{v,j,\Omega \rightarrow v',j',\Omega'}^J(E) \right|^2 \end{aligned} \quad (23)$$

as the state-to-state integral cross section.

III. RESULTS

A. Calculation details

The calculations have been performed employing the BKMP2³⁴ surface and the 4 hierarchical surfaces, A2, A3, A4, CCI, of Mielke, Garrett and Peterson.³⁶ The barrier heights on these surfaces are 0.417 eV (BKMP2), 0.403 eV (A2), 0.421 eV (A3), 0.419 eV (A4) and 0.417 eV (CCI). The zero point energies of the reactants are 0.2702 eV (BKMP2), 0.2666 eV

(A2), 0.2699 eV (A3), 0.2700 eV (A4) and 0.2703 eV (CCI). Results have been obtained for a range of total energies from 0.4 eV to 1.2 eV. A double exponential damping operator⁴¹ has been used. The form of the damping operator was taken to be $\hat{A} = A_R(R)A_r(r)$ with $A_x(x) = \exp[-c_{\text{abs}} \exp(-2(x_{\text{max}} - x_{\text{abs}})/(x - x_{\text{abs}}))]$ for $x > x_{\text{abs}}$ and $\hat{A} = 1$ otherwise, where $x = R$ or r . The parameter c_{abs} controls the strength of the absorption and $(x_{\text{max}} - x_{\text{abs}})$ is the length of the absorption region. In the calculations 50 angular DVR grid points were used. However, the final wavepacket was analysed to extract the **S** matrix elements for the lowest 3 vibrational states and the lowest 30 rotational states. The initial conditions used for all the calculations set the initial state of the reactants to $(v,j,\Omega)=(0,0,0)$. All parameters used in the calculations are listed in Table I. Most of the calculations required 2500 iteration steps to converge the results which corresponds to about 50 minutes computational time on a SunFire V60x dual Xeon sever cluster using one processor per (J, Ω') set.

In the calculations presented in this work **S** matrix elements for $J=0-24$ have been obtained. The calculations were performed in several batches, including several values of J in one calculation. The separate calculations have been analysed separately to obtain the **S** matrix elements for each value of J . The **S** matrix elements are then written into one big data file which is read by two programs that calculate the state-to-state integral cross sections and the state-to-state differential cross sections using the above formulae. In this way total integral and differential cross sections have been obtained and state-to-state integral and differential cross sections for $v' = 0, 1$ and $j' = 0, 2, 4, 6$.

Calculations were also performed employing the ABC code³⁷ for the BKMP2 surface only to verify our DiffRealWave results. The parameters used in the ABC calculations are listed in Table II. We also performed calculations with $j_{\text{max}}=20$ and $k_{\text{max}}=10$ but did not see any significant changes in the results for the energy range considered in this paper.

B. Comparison of DiffRealWave and ABC results

Figure 1 shows the state-to-state differential cross sections calculated on the BKMP2 surface for two angles, 0° and 90° , for $v' = 0, 1$ and $j' = 0, 2, 4, 6$ versus total energy in eV. The solid and broken lines are the results from our DiffRealWave code and the symbols represent the results from the ABC code. The agreement is very good over the energy range shown.

Figure 2 shows the state-to-state differential cross sections calculated employing the BKMP2 surface for two energies, 0.796 eV and 1.016 eV for $v' = 0$ and 1.016 eV and 1.2 eV for $v' = 1$, versus scattering angle θ . As in Figure 1 results for $j' = 0, 2, 4, 6$ are shown and the lines correspond to the DiffRealWave results while the symbols correspond to the ABC ones. Here also the agreement is very good.

We chose energies similar to those used by Althorpe³⁹ at which to present the results so as to be able to compare with his results. The results in Figure 1 should be compared to the corresponding results in Figures 7 and 8 and the results in Figure 2 to those in Figure 9 in Ref. 39. The excellent agreement of our results with the ones from the ABC code and the ones in Ref. 39, all employing the BKMP2 surface, verify the accuracy of the DiffRealWave code.

The above results are for the BKMP2 surface only. The next two sections present our new results obtained with the new DiffRealWave code employing the A2, A3, A4 and CCI surfaces.

C. Integral cross sections

In this section we present integral cross sections for the five different potential energy surfaces employed in this study. Figure 3 shows the integral cross sections summed up over all product states ($v' = 0 - 3$ and $j' = 0 - 29$) for all five PES. One can clearly see that the results from the A3, A4, CCI and the BKMP2 surface are nearly the same, especially for energies above ≈ 0.9 eV. The inset shows a close up of the low energy region of the plot. Here one can distinguish the different curves. The A3 curve is the lowest, then the A4, then the CCI, BKMP2 and the highest curve is from the A2 PES. The total integral cross section obtained using the A2 PES is the largest for the whole energy range considered here.

We now look at the state-to-state integral cross sections. Figure 4 shows the integral cross sections for different product quantum states for the different surfaces. Figure 4(a) shows the integral cross sections for $v' = 0$ and $j' = 0, 2, 4, 6$ obtained from the A3, A4 and the CCI surfaces. These results confirm the findings from Figure 3 that calculations employing the A3, A4 and the CCI surfaces produce very similar results. The findings for $v' = 1$ are the same and we do not show them here.

Figure 4(b) shows the integral cross sections for $v' = 0$ and $j' = 0, 2, 4, 6$ that were

obtained using the BKMP2, A2 and CCI surfaces. As seen in Figure 3 the results from the A2 surface are largest for the energy range shown. Only for energies close to the high end of the range, i.e. 1.2 eV, does the difference get smaller. Between 1.1 eV and 1.2 eV the results from all three surfaces agree well in the case of $v' = j' = 0$ and $v' = 0, j' = 2$. It also seems that the features like dips and peaks are shifted to lower energies in the results from the A2 surface when compared to the ones from the other two surfaces. Figure 4(c) shows the integral cross sections obtained on the BKMP2, A2 and CCI surface for $v' = 1$ and $j' = 0, 2, 4, 6$. Also in this figure the results from the A2 surfaces are the largest in magnitude. And again the shift of some of the features to lower energies is visible in this figure.

The findings for the results from the CCI surface compared to those from the BKMP2 surface are not so clear. For $(v', j') = (0, 0), (0, 2), (1, 0)$ the results from the CCI surface are smaller than the results from the BKMP2 surface. But for the other states shown the results are larger.

The results obtained for the A2 surface can be explained by the difference in barrier height, which is the lowest for all five surfaces considered in this work. Also the thresholds for the population of the different vibrational rotational states are shifted to lower energies. The difference in the results from CCI and the BKMP2 surface cannot be explained so easily. The barrier height for the BKMP2 and the CCI surface is virtually the same and also the H-H distance is very similar.³⁶ One marked difference, apart from possible very subtle differences, is the van der Waals well. Again the H-H distance on the BKMP2 and the CCI surface are very similar but the well on the BKMP2 surface is deeper by about $14\mu E_h$ than the well on the CCI surface.³⁶ But the results from the CCI and the BKMP2 surface for the integral cross sections are in quite good agreement so that the small differences are not likely to give preference to one surface or the other.

D. State-to-state differential cross sections

We will now look at the more detailed state-to-state differential cross sections from the different surfaces to see if the differences can be seen at this level of detail.

Figure 5 shows the differential cross sections for different product states with $v' = 0$ for selected angles and energies. Figure 5(a) shows the differential cross sections for $j' = 0, 2, 4, 6$

and $\theta = 0^\circ, 90^\circ, 180^\circ$ versus total energy. We only show the results for the BKMP2, A2 and CCI surface. The results from the A3 and the A4 surface are nearly the same as the ones from the CCI surface and therefore have been omitted here. Also at this level of detail the differential cross sections obtained from the A2 surface are larger over the energy range considered here than the results from the other two surfaces. In fact the results from the BKMP2 and the CCI surface are very similar. Only for $v' = 0, j' = 0, 2, 4, \theta = 0^\circ$ and $v' = 0, j' = 0, 6, \theta = 180^\circ$ one can see some differences between the results from BKMP2 and the CCI surfaces.

Figure 5(b) shows the differential cross sections for $j' = 0, 2, 4, 6$ and $E = 0.796$ eV, 1.016 eV, 1.2 eV versus scattering angle θ . Also in this figure it is clear that the results obtained on the A2 surface are larger than the results from the calculations which employed the BKMP2 and CCI surfaces. Again the results from the BKMP2 and the CCI surface are nearly identical.

Figure 6 shows the differential cross section for different product states with $v' = 1$ for selected angles and energies. Figure 6(a) shows the differential cross sections for $j' = 0, 2, 4$ and $\theta = 0^\circ, 90^\circ, 180^\circ$ versus total energy. We omit the results for $j' = 6$ because the magnitude is too small to be shown in the energy range we consider in this work. Figure 6(b) shows the differential cross sections for $j' = 0, 2, 4$ and $E = 1.016$ eV and 1.2 eV versus scattering angle θ . Results for $E = 0.796$ eV are not shown here, as they were in the corresponding figure for $v' = 0$, as the magnitude is too small to be displayed. Again for the $v' = 1$ case, the results from the A2 surface are largest and the results from the BKMP2 and CCI surface agree quite well, though there seem to be some detectable differences for $(v' = 1, j' = 4)$ at 1.2 eV.

IV. CONCLUSIONS AND OUTLOOK

This article reports quantum scattering calculations for the $\text{H} + \text{H}_2 \rightarrow \text{H}_2 + \text{H}$ exchange reaction on five different potential energy surfaces. The calculations have been performed using a new parallel code, DiffRealWave, which is based on the real wavepacket approach by Gray and Balint-Kurti. The calculations have been parallelised over the helicity quantum number, Ω , so as to perform the calculations for each set J, Ω on a separate processor and to facilitate the calculations.

State-to-state integral as well as differential cross sections for $v' = 0, 1$ and $j' = 0, 2, 4, 6$ are presented. Calculations using the DiffRealWave code and the ABC code employing the BKMP2 surface yielded results which were in excellent agreement with each other, confirming the accuracy of our new code.

The BKMP2 surface has been used in numerous theoretical studies of the $\text{H} + \text{H}_2$ reaction and its isotopic variants and results have been in very good agreement with the experimental results. It has been regarded as the most accurate surface so far. Four years ago Mielke and co-workers calculated a hierarchical family of four *ab initio* potential energy surfaces ranging in quality from double-zeta to the complete basis set limit (obtained by extrapolation). The complete basis set surface, CCI surface, should be the most accurate surface to date. We performed calculations for all five surfaces, BKMP2, A2, A3, A4 and CCI, to investigate the sensitivity of integral and differential cross sections to subtle differences in the potential energy surface. Our state-to-state differential cross sections are the first reported employing the A2, A3, A4 and CCI surfaces for the H_3 system.

The differences between the results from the A3, A4 and CCI surfaces are hardly noticeable. All three surfaces produce results in very close agreement. The cross sections from the A2 surface are consistently larger than those from the other surfaces over the energy range examined and differ noticeably from them. Also several features in the integral and the differential cross sections are shifted to slightly lower energies.

The most surprising conclusion however is that the results from the BKMP2 and the CCI surface agree extremely well. At the quantum state resolved differential cross sections level of detail some small differences can be seen but mainly in magnitude only. A shift in energy of the general features, such as peaks and dips of the cross section, are not observed, in contrast to the situation for the A2 surface.

We are now in the process of extending our calculations to the isotopic variants of the hydrogen exchange reaction to be able to compare our findings with results from experiments. Also calculations to cover energies above 1.2 eV are in preparation.

A manuscript is currently in preparation which will outline more details with regards to the DiffRealWave code. We will report on the details of the parallelisation and the scaling with increasing J .

In the development of the DiffRealWave program we have kept in mind its future application to more complex reactions which may involve a deep well. Our limiting procedure

of the Coriolis coupling potential stems from these considerations. Future work will include the application of the DiffRealWave code to systems such as $O(^1D)+H_2$.

Acknowledgments

The calculations reported in this paper have been performed on the CMS computational facility housed by the CCMS at the University of Queensland. The computational facilities have been purchased from funds provided by the University of Queensland and the Smart State Research Facilities Fund. MH would like to thank Professors J.N.L. Connor, E.M. Goldfield, M. Shapiro and Dr. A.J.H.M. Meijer for helpful discussions. SKG was supported by the U.S. Department of Energy, Office of Basic Energy Sciences, Division of Chemical Sciences, Geosciences, and Biosciences under DOE contract W-31-109-ENG-38. MH would like to thank Sun Microsystems for funding.

* Author to whom correspondence should be addressed. Email. m.hankel@uq.edu.au

† Electronic address: s.smith@uq.edu.au

‡ Electronic address: r.j.allan@daresbury.ac.uk

§ Electronic address: gray@tcg.anl.gov

¶ Electronic address: Gabriel.Balint-Kurti@Bristol.ac.uk

- ¹ J.-C. Nieh and J. Valentini, Phys. Rev. Lett. **60**, 519 (1988).
- ² D. E. Adelman, N. E. Shafer, D. A. V. Kliner, and R. N. Zare, J. Chem. Phys. **97**, 7323 (1992).
- ³ D. Neuhauser, R. S. Judson, D. J. Kouri, D. E. Adelman, N. E. Shafer, D. A. V. Kliner, and R. N. Zare, Science **257**, 519 (1992).
- ⁴ T. N. Kitsopoulos, M. A. Buntine, D. P. Baldwin, R. N. Zare, and D. W. Chandler, Science **260**, 1605 (1993).
- ⁵ E. Wrede, L. Schnieder, K. H. Welge, F. J. Aoiz, L. Bañares, J. F. Castillo, and B. Martínez-Haya, J. Chem. Phys. **110**, 9971 (1999).
- ⁶ F. Fernández-Alonso, B. D. Bean, J. D. Ayers, A. E. Pomerantz, R. N. Zare, L. Bañares, and F. J. Aoiz, Angewandte Chemie Intl. Ed. **39**, 2748 (2000).
- ⁷ S. A. Harich, D. Dai, C. C. Wang, X. Yang, S. D. Chao, and R. T. Skodje, Nature **419**, 281 (2002).
- ⁸ S. A. Harich, D. Dai, X. Yang, S. D. Chao, and R. T. Skodje, J. Chem. Phys. **116**, 4769 (2002).
- ⁹ D. Dai, C. C. Wang, S. A. Harich, X. Wang, X. Yang, S. D. Chao, and R. T. Skodje, Science **300**, 1730 (2003).
- ¹⁰ F. Ausfelder, A. E. Pomerantz, R. N. Zare, S. C. Althorpe, F. J. Aoiz, L. Bañares, and J. F. Castillo, J. Chem. Phys. **120**, 3255 (2004).
- ¹¹ A. E. Pomerantz, F. Ausfelder, R. N. Zare, S. C. Althorpe, F. J. A. L. Bañares, and J. F. Castillo, J. Chem. Phys. **120**, 3244 (2004).
- ¹² A. E. Pomerantz, F. Ausfelder, R. N. Zare, J. C. Juanes-Marcos, S. C. Althorpe, V. S. Rábanos, F. J. Aoiz, L. Bañares, and J. F. Castillo, J. Chem. Phys. **121**, 6587 (2004).
- ¹³ K. Koszinowski, N. T. Goldberg, A. E. Pomerantz, R. N. Zare, J. C. Juanes-Marcos, and S. C. Althorpe, J. Chem. Phys. **123**, 054306 (2005).
- ¹⁴ G. C. Schatz and A. Kuppermann, Phys. Rev. Lett. **35**, 1266 (1975).

- ¹⁵ G. C. Schatz and A. Kuppermann, *J. Chem. Phys.* **65**, 4668 (1976).
- ¹⁶ J. C. Sun, B. H. Choi, R. T. Poe, and K. T. Tang, *Phys. Rev. Lett.* **44**, 1211 (1980).
- ¹⁷ K. Haug, D. W. Schwenke, Y. Shima, D. G. Truhlar, J. Zhang, and D. J. Truhlar, *J. Phys. Chem.* **90**, 6757 (1986).
- ¹⁸ S. C. Althorpe, F. Fernández-Alonso, B. D. Bean, J. D. Ayers, A. E. Pomerantz, R. N. Zare, and E. Wrede, *Nature* **416**, 67 (2002).
- ¹⁹ S. L. Mielke, K. A. Peterson, D. W. Schwenke, B. C. Garret, D. G. Truhlar, J. V. Michael, M.-C. Su, and J. W. Sutherland, *Phys. Rev. Lett.* **91**, 063201 (2003).
- ²⁰ J. V. Michael, M.-C. Su, and J. W. Sutherland, *J. Phys. Chem.* **108**, 432 (2004).
- ²¹ J. C. Juanes-Marcos, S. C. Althorpe, and E. Wrede, *Science* **309**, 1195 (2005).
- ²² J. Vaníček, W. H. Miller, J. Castillo, and F. Aoiz, *J. Chem. Phys.* **123**, 054108 (2005).
- ²³ Y. Zheng, *J. Chem. Phys.* **122**, 094316 (2005).
- ²⁴ J. C. Juanes-Marcos and S. C. Althorpe, *J. Chem. Phys.* **122**, 204324 (2005).
- ²⁵ S. C. Althorpe, *J. Chem. Phys.* **124**, 084105 (2006).
- ²⁶ F. J. Aoiz, L. Bañares, and V. J. Herrero, *Int. Rev. Phys. Chem* **24**, 119 (2005).
- ²⁷ P. Casavecchia, *Rep. Prog. Phys.* **63**, 355 (2000).
- ²⁸ K. Liu, *Annu. Rev. Phys. Chem.* **52**, 139 (2001).
- ²⁹ S. C. Althorpe and D. C. Clary, *Annu. Rev. Phys. Chem.* **54**, 493 (2003).
- ³⁰ D. G. Truhlar and C. J. Horowitz, *J. Chem. Phys.* **68**, 2466 (1978).
- ³¹ D. G. Truhlar and C. J. Horowitz, *J. Chem. Phys.* **71**, 1514 (1979).
- ³² A. J. C. Varandas, F. B. Brown, C. A. Mead, D. G. Truhlar, and N. C. Blais, *J. Chem. Phys.* **86**, 6258 (1987).
- ³³ A. I. Boothroyd, W. J. Keogh, P. G. Martin, and M. R. Peterson, *J. Chem. Phys.* **95**, 4343 (1991).
- ³⁴ A. I. Boothroyd, W. J. Keogh, P. G. Martin, and M. R. Peterson, *J. Chem. Phys.* **104**, 7139 (1996).
- ³⁵ Y.-S. M. Wu, A. Kuppermann, and J. B. Anderson, *Phys. Chem. Chem. Phys.* **1**, 929 (1999).
- ³⁶ S. L. Mielke, B. C. Garrett, and K. A. Peterson, *J. Chem. Phys.* **116**, 4142 (2002).
- ³⁷ D. Skouteris, J. F. Castillo, and D. E. Manolopoulos, *Comput. Phys. Commun.* **133**, 128 (2000).
- ³⁸ N. Balucani, P. Casavecchia, L. Bañares, F. J. Aoiz, T. Gonzalez-Lezana, P. Honvault, and J.-M. Launay, *J. Phys. Chem.* **110**, 817 (2006).

- ³⁹ S. C. Althorpe, J. Chem. Phys. **114**, 1601 (2001).
- ⁴⁰ K. Yuan, Y. Cheng, X. Liu, S. Harich, X. Yang, and D. H. Zhang, Phys. Rev. Lett. **96**, 103202 (2006).
- ⁴¹ S. K. Gray and G. G. Balint-Kurti, J. Chem. Phys. **108**, 950 (1998).
- ⁴² M. Hankel, S. K. Gray, and G. G. Balint-Kurti, the DiffRealWave code is available on request from M. Hankel, email: m.hankel@uq.edu.au.
- ⁴³ M. Hankel, G. G. Balint-Kurti, and S. K. Gray, J. Chem. Phys. **113**, 9658 (2000).
- ⁴⁴ M. Hankel, G. G. Balint-Kurti, and S. K. Gray, J. Phys. Chem. **105**, 2330 (2001).
- ⁴⁵ S. K. Gray, G. G. Balint-Kurti, G. C. Schatz, J. J. Lin, X. Liu, S. Harich, and X. Yang, J. Chem. Phys. **113**, 7330 (2000).
- ⁴⁶ S. K. Gray, C. Petrongolo, K. Drukker, and G. C. Schatz, J. Phys. Chem. **103**, 9448 (1999).
- ⁴⁷ S. K. Gray, E. M. Goldfield, G. C. Schatz, and G. G. Balint-Kurti, Phys. Chem. Chem. Phys. **1**, 1141 (1999).
- ⁴⁸ G. G. Balint-Kurti, A. I. Gonzalez, E. M. Goldfield, and S. K. Gray, Faraday Discuss. **110**, 169 (1998).
- ⁴⁹ F. Gögtas, Chem. Phys. Lett. **425**, 157 (2006).
- ⁵⁰ P. Gamallo, R. Sayós, M. Gonzáles, C. Petrongolo, and P. Defazio, J. Chem. Phys. **124**, 174303 (2006).
- ⁵¹ W. L. Wang, C. Rosa, and J. Brandão, Chem. Phys. Lett. **418**, 250 (2006).
- ⁵² A. R. Edmonds, *Angular Momentum in Quantum Mechanics* (Princeton University Press, Princeton, New Jersey, 1960).
- ⁵³ R. N. Zare, *Angular Momentum* (John Wiley and Sons, New York, 1988).
- ⁵⁴ G. G. Balint-Kurti, R. N. Dixon, and C. C. Marston, Internat. Rev. Phys. Chem. **11**, 317 (1992).
- ⁵⁵ A. R. Offer and G. G. Balint-Kurti, J. Chem. Phys. **101**, 10416 (1994).
- ⁵⁶ G. G. Balint-Kurti, Adv. Chem. Phys. **128**, 249 (2003).
- ⁵⁷ R. T Pack, J. Chem. Phys. **60**, 633 (1974).
- ⁵⁸ M. Shapiro and G. G. Balint-Kurti, J. Chem. Phys. **71**, 1461 (1979).
- ⁵⁹ G. G. Balint-Kurti and M. Shapiro, Chem. Phys. **61**, 137 (1981).
- ⁶⁰ G. G. Balint-Kurti, L. Füsti-Molnár, and A. Brown, Phys. Chem. Chem. Phys. **3**, 702 (2001).
- ⁶¹ E. M. Goldfield and S. K. Gray, Comp. Phys. Commun. **84**, 1 (1996).
- ⁶² C. Leforestier, J. Chem. Phys. **94**, 6388 (1991).

- ⁶³ G. Corey and D. Lemoine, J. Chem. Phys. **97**, 4115 (1992).
- ⁶⁴ J. C. Light, I. P. Hamilton, and V. J. Lill, J. Chem. Phys. **82**, 1400 (1985).
- ⁶⁵ G. G. Balint-Kurti, in *International Review of Science, Series II*, edited by A. D. Buckingham and C. A. Coulson (Butterworth, London, 1975), Vol. 1, pp. 286–326.
- ⁶⁶ A. J. H. M. Meijer, E. M. Goldfield, S. K. Gray, and G. G. Balint-Kurti, Chem. Phys. Lett. **293**, 270 (1998).
- ⁶⁷ M. Hankel, G. G. Balint-Kurti, and S. K. Gray, Int. J. Quant. Chem. **92**, 205 (2003).
- ⁶⁸ I. Miquel, M. González, R. Sayós, G. G. Balint-Kurti, S. K. Gray, and E. M. Goldfield, J. Chem. Phys. **118**, 3111 (2003).
- ⁶⁹ G. G. Balint-Kurti, R. N. Dixon, and C. C. Marston, J. Chem. Soc. Faraday Trans. **86**, 1741 (1990).
- ⁷⁰ I. S. Gradshteyn and I. M. Ryzhik, *Table of Integrals, Series and Products*, 4th ed. (Academic Press, New York, 1965).

TABLE I: Grid and initial condition details for the DiffRealWave calculations for H+H₂ for non-zero total angular momentum employing the BKMP2, A2, A3, A4 and CCI surfaces.^a

scattering coordinate (R) range/ a_0	0.2-12.5
number of grid points in R	127
internal coordinate (r) range/ a_0	0.5-11.5
number of grid points in r ,	119
number of angular grid points	50
absorption region length in R and r/a_0	4 (4)
absorption strength (c_{abs})	2.0
centre of initial wavepacket (R_0)/ a_0	6
width of the wavepacket, α	8.0
smoothing of the wavepacket, β	0.5
initial translational energy, $E_{\text{trans}}/\text{eV}$	0.7
cut-off energy, V_{cut}/a_0	0.22
Hamiltonian scaling parameter, BKMP2 a_s^b	0.874965
Hamiltonian scaling parameter, A2 a_s^b	0.874971
Hamiltonian scaling parameter, A3 a_s^b	0.874972
Hamiltonian scaling parameter, A4 a_s^b	0.874976
Hamiltonian scaling parameter, CCI a_s^b	0.874974
Hamiltonian shift parameter, all b_s^b	-0.991250

^a All quantities are given in atomic units.

^b These parameters are computed automatically by the computer code. a_s has the units 1/eV and b_s is dimensionless.

TABLE II: Grid and initial condition details for the ABC calculations for H+H₂ for non-zero total angular momentum employing the BKMP2 surface.

total angular momentum quantum numbers, J	0 - 24
maximum rotational quantum number of any channel, $jmax$	16
helicity truncation parameter, $kmax$	5
maximum hyperradius $rmax$,	12.0 a_0
maximum internal energy in any channel, $emax$	2.5 eV
initial scattering energy	0.4 eV
scattering energy increment	0.002 eV
total number of scattering energies	551
maximum value of v'	1
maximum value of j'	10

FIG. 1: Differential cross sections calculated for the BKMP2 PES presented at two fixed scattering angles, $\theta = 0^\circ$ and $\theta = 90^\circ$, versus total energy (eV) for four different product quantum states. The solid and broken lines are the results from the DiffRealWave code and the symbols represent results obtained with the ABC code.

FIG. 2: Differential cross sections calculated for the BKMP2 PES versus scattering angle θ for different product quantum states and energies. The solid and broken lines are the results from the DiffRealWave code and the symbols represent results obtained with the ABC code.

FIG. 3: Total integral cross sections for the BKMP2, A2, A3, A4 and CCI surface.

FIG. 4: State-to-state integral cross section for the BMKP2, A2, A3, A4 and CCI surface. (a) Integral cross sections for the A3, A4 and CCI surfaces for $v' = 0$ and $j' = 0, 2, 4, 6$. (b) Integral cross sections for the BMKP2, A2 and CCI surfaces for $v' = 0$ and $j' = 0, 2, 4, 6$. (c) Integral cross sections for the BMKP2, A2 and CCI surfaces for $v' = 1$ and $j' = 0, 2, 4, 6$.

FIG. 5: Selected state-to-state differential cross section for the $v' = 0$ product quantum state for surfaces BMKP2, A2 and CCI. (a) Differential cross sections for $(v' = 0, j' = 0, 2, 4, 6)$ for three scattering angles, $\theta = 0^\circ$, 90° and 180° versus total energy (eV). (b) Differential cross sections for $(v' = 0, j' = 0, 2, 4, 6)$ for three total energies, 0.796 eV, 1.016 eV and 1.2 eV, versus scattering angle θ .

FIG. 6: Selected state-to-state differential cross section for the $v' = 1$ product quantum state for surfaces BMKP2, A2 and CCI. (a) Differential cross sections for $(v' = 1, j' = 0, 2, 4)$ for three angles, $\theta = 0^\circ$, 90° and 180° versus total energy (eV). (b) Differential cross sections for $(v' = 0, j' = 0, 2, 4)$ for two total energies, 1.016 eV and 1.2 eV, versus scattering angle θ .

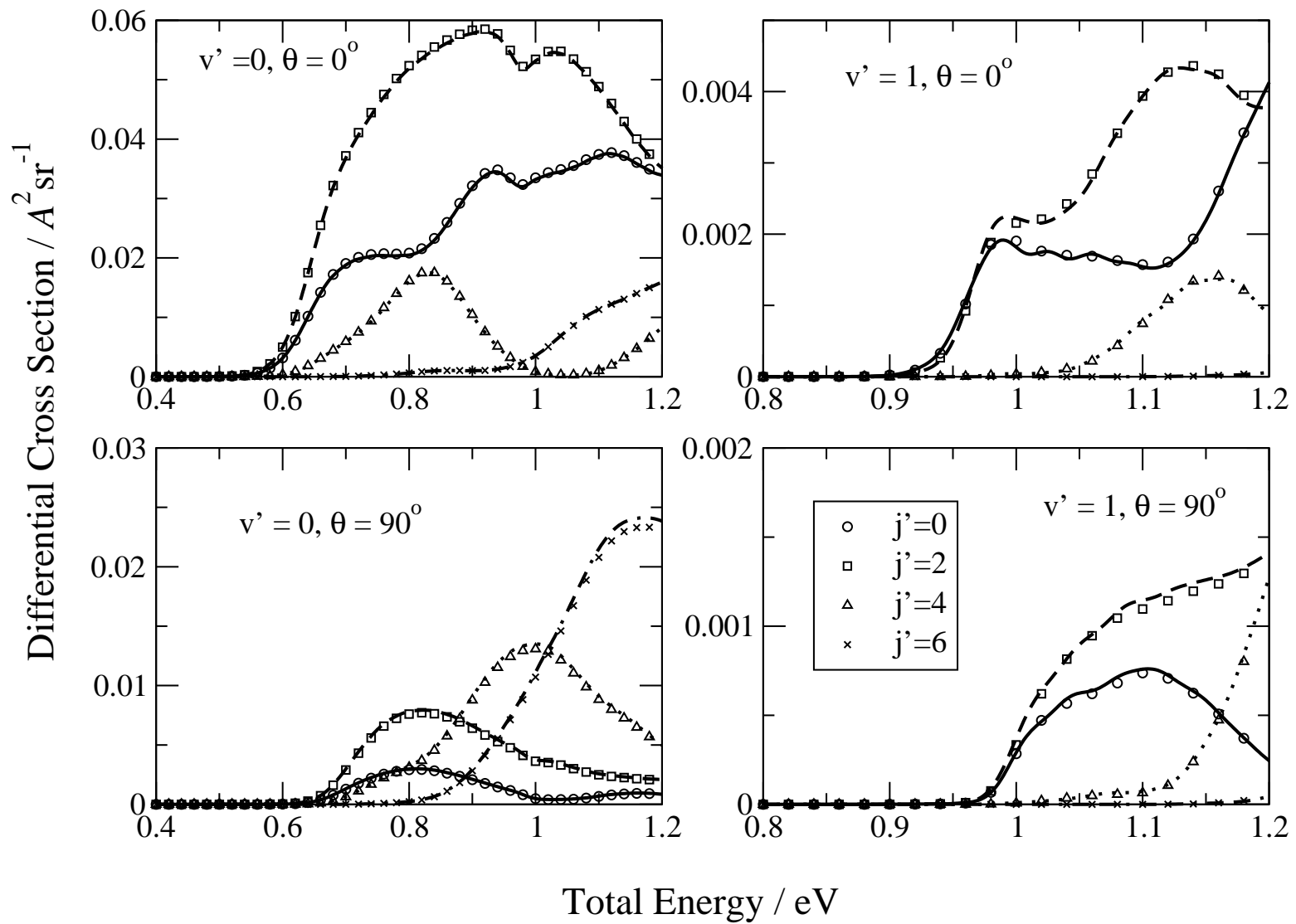


Figure 1

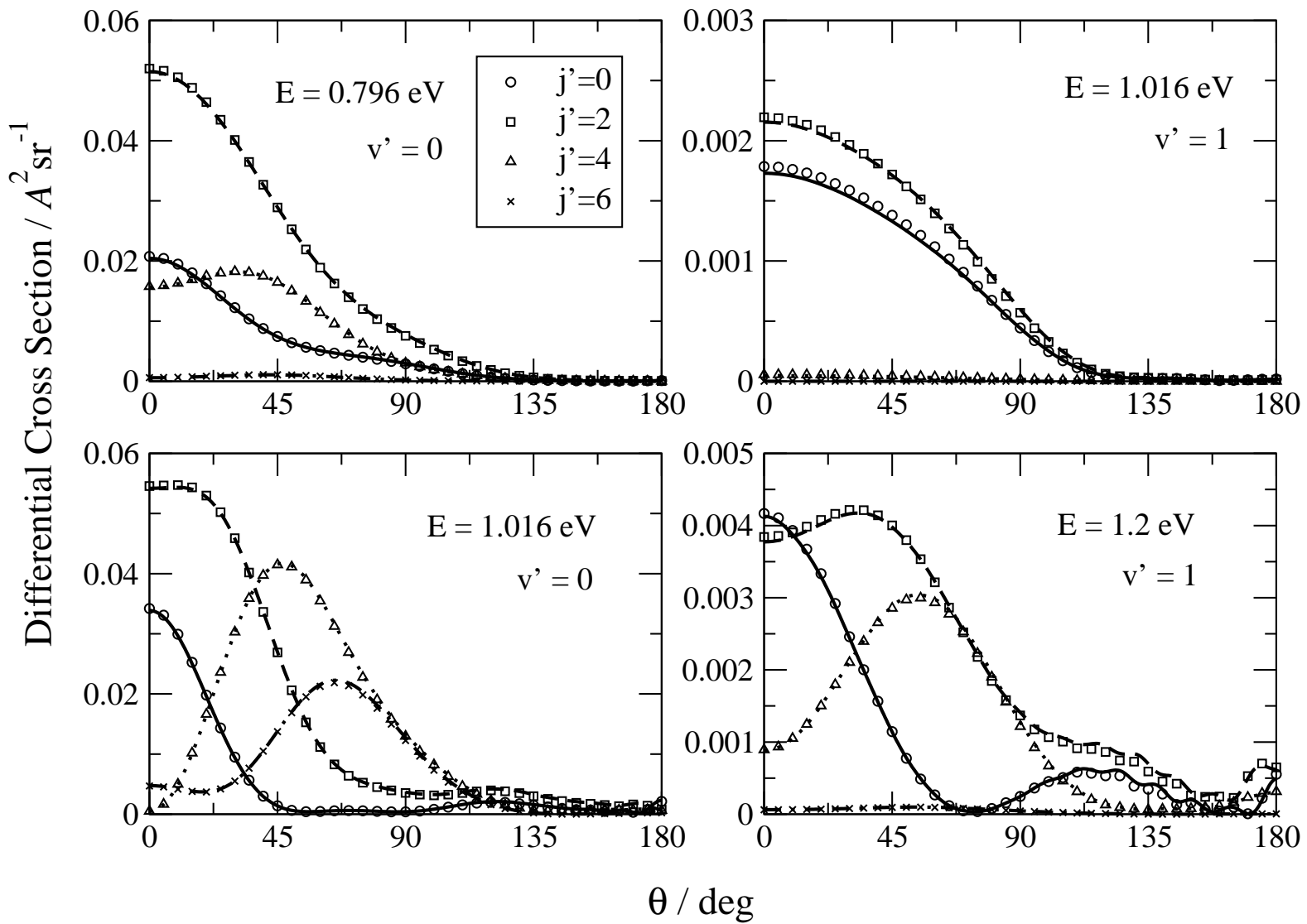


Figure 2

Figure 3

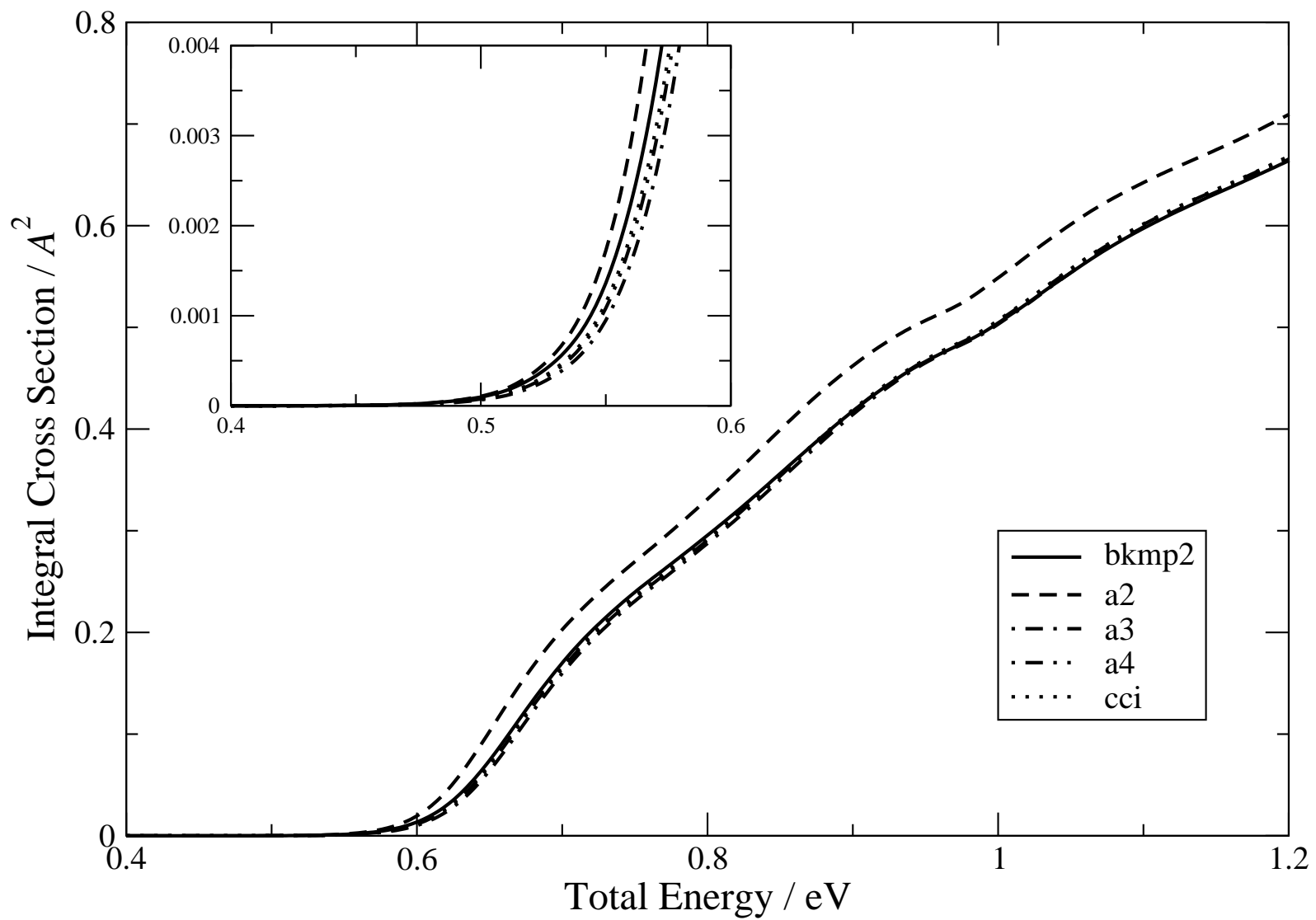


Figure 4(a)

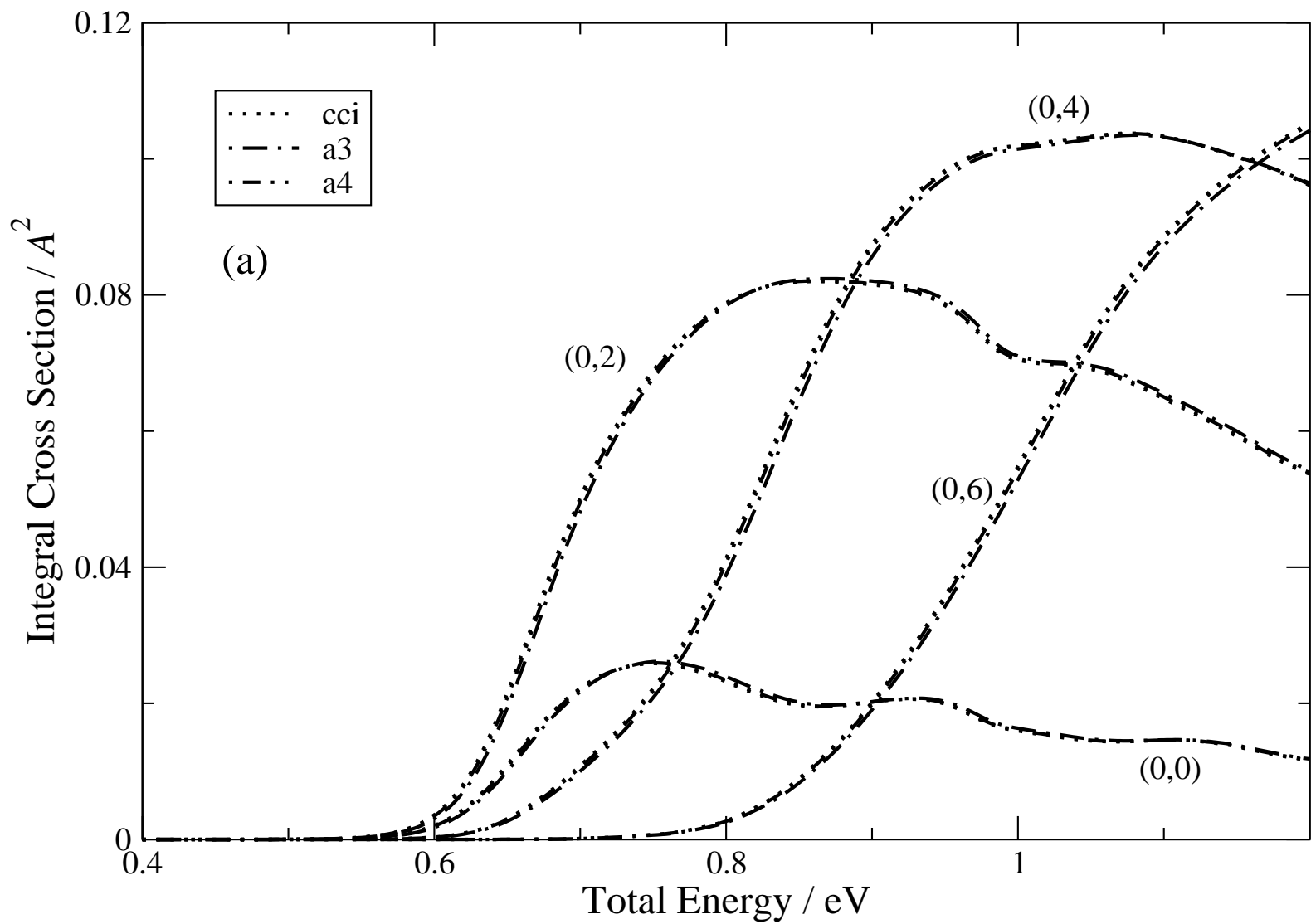
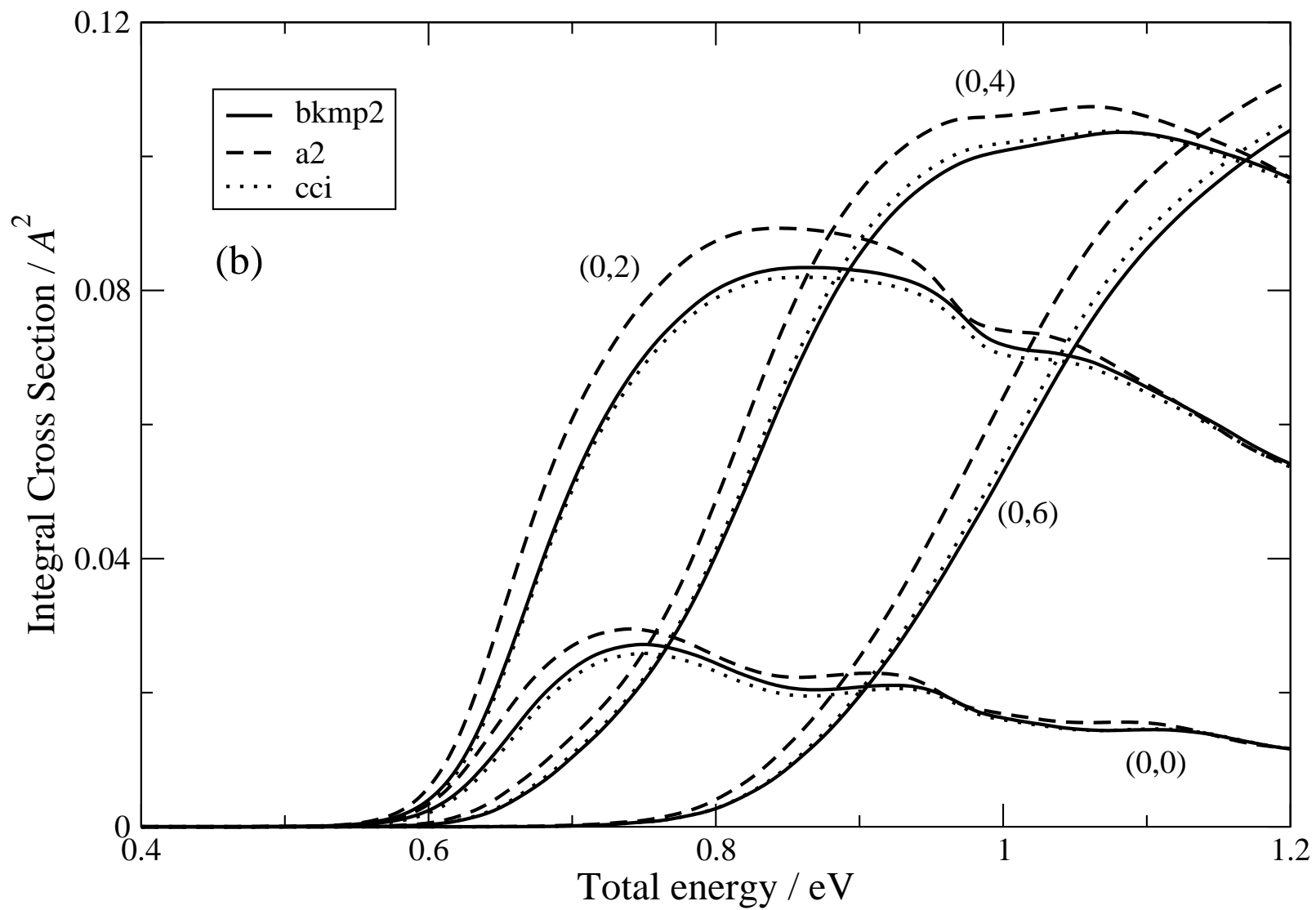


Figure 4(b)



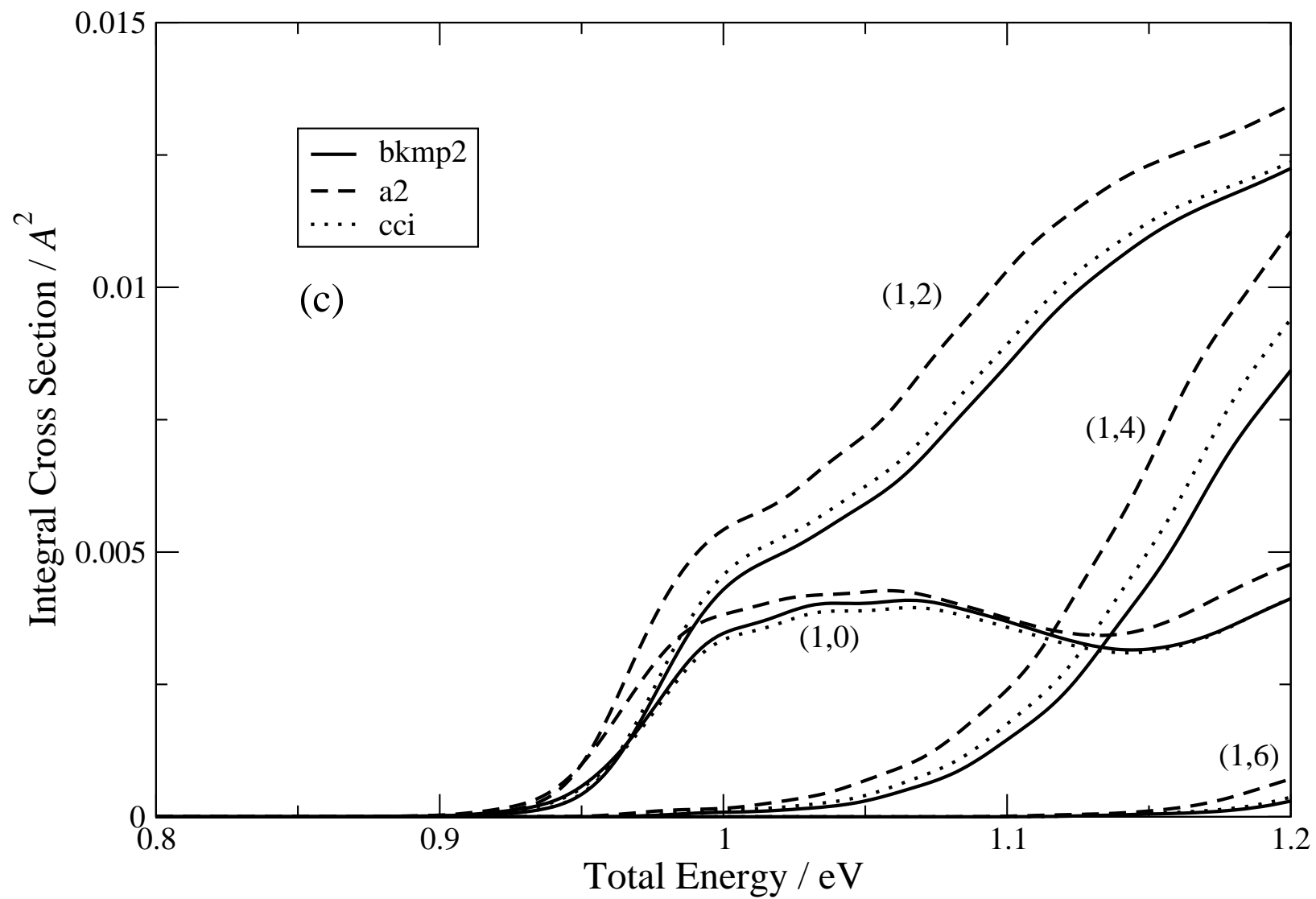


Figure 4(c)

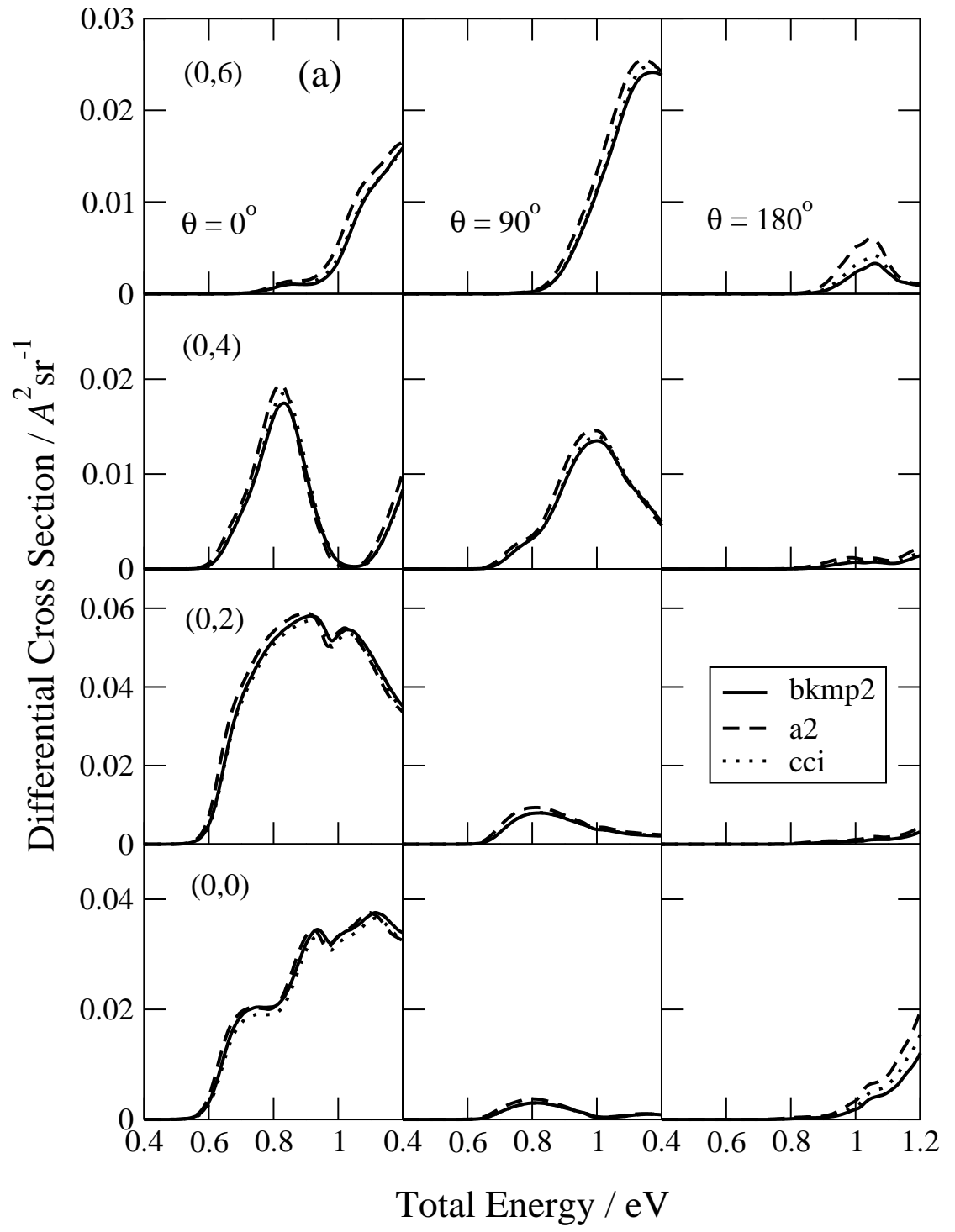


Figure 5(a)

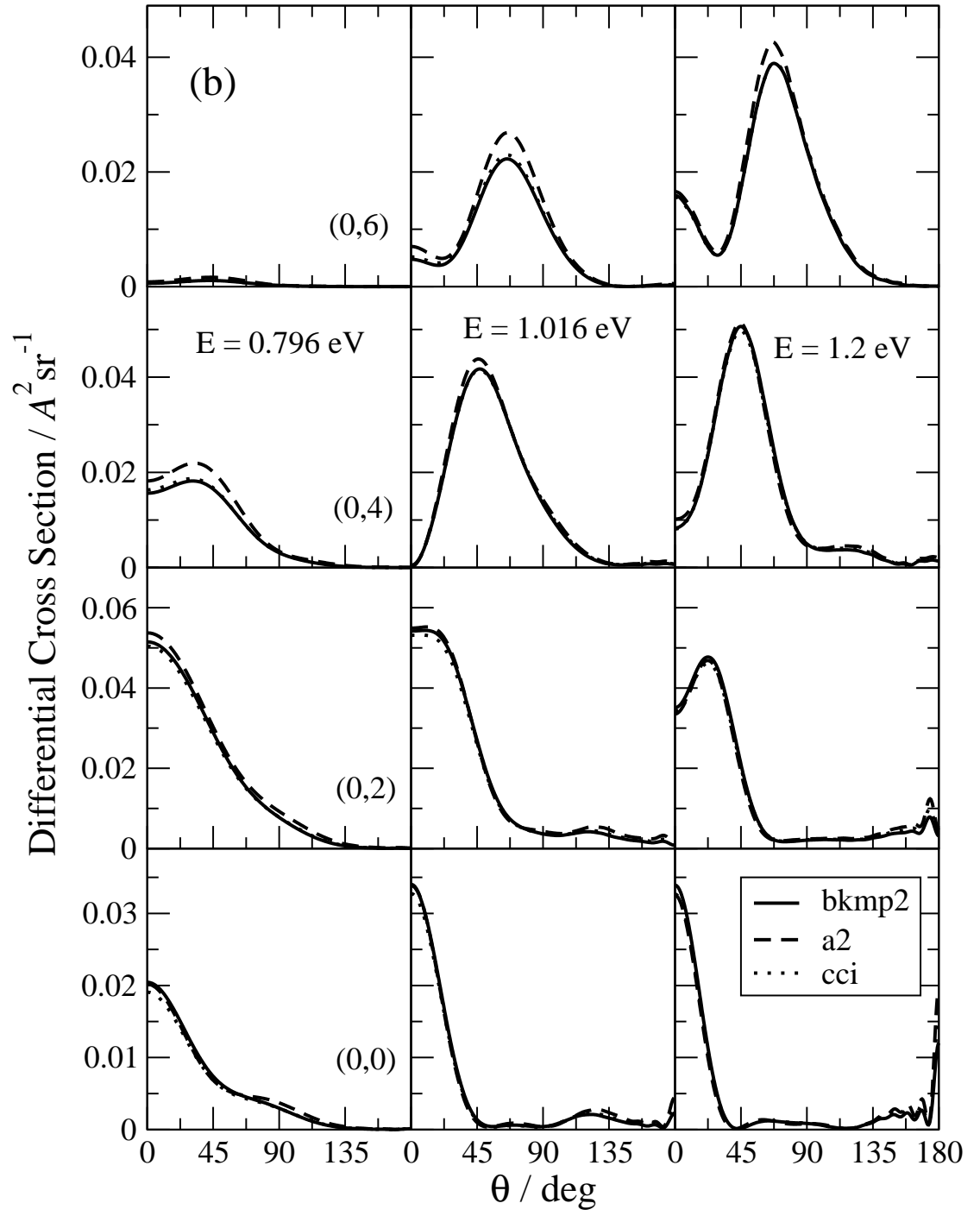


Figure 5(b)

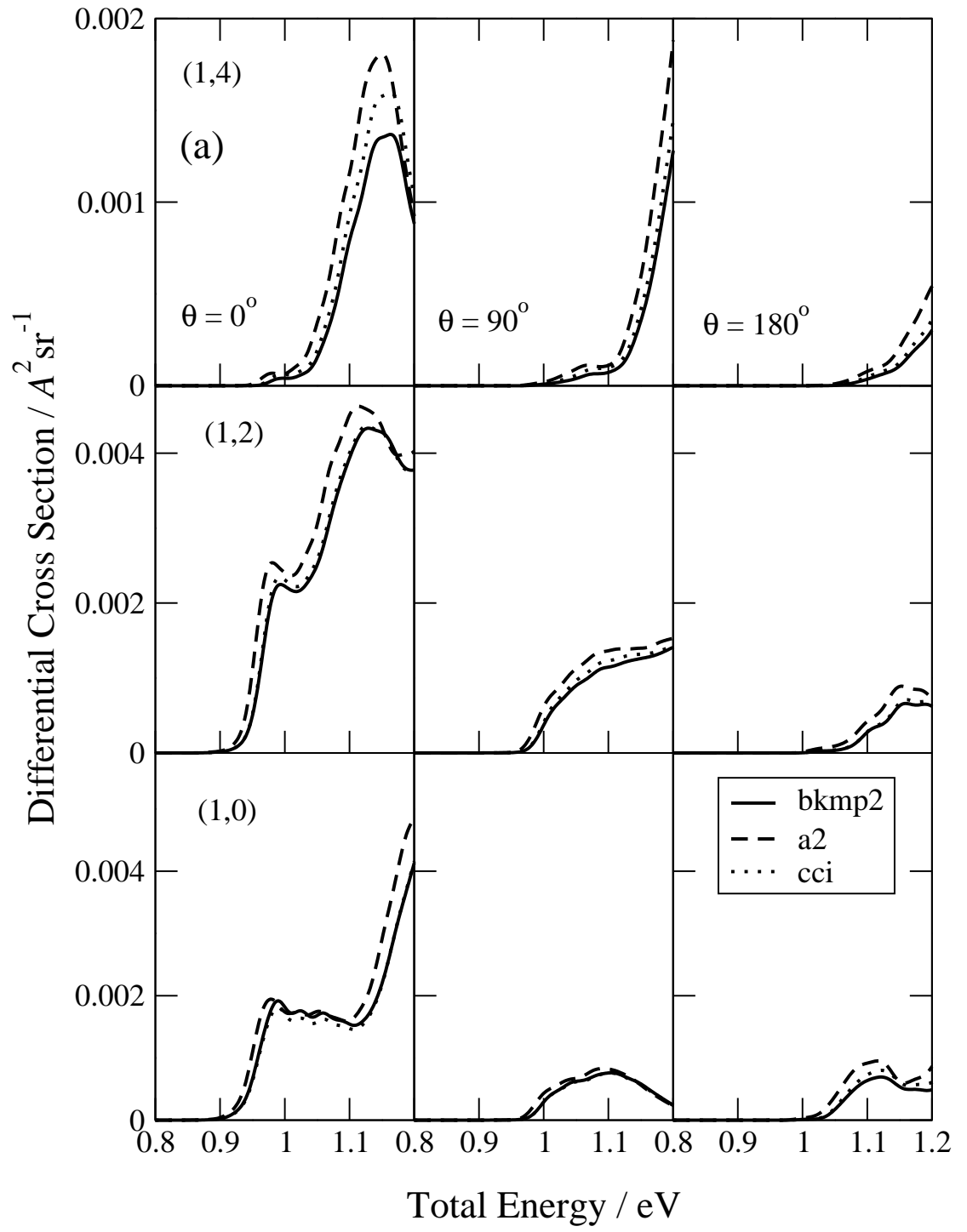


Figure 6(a)

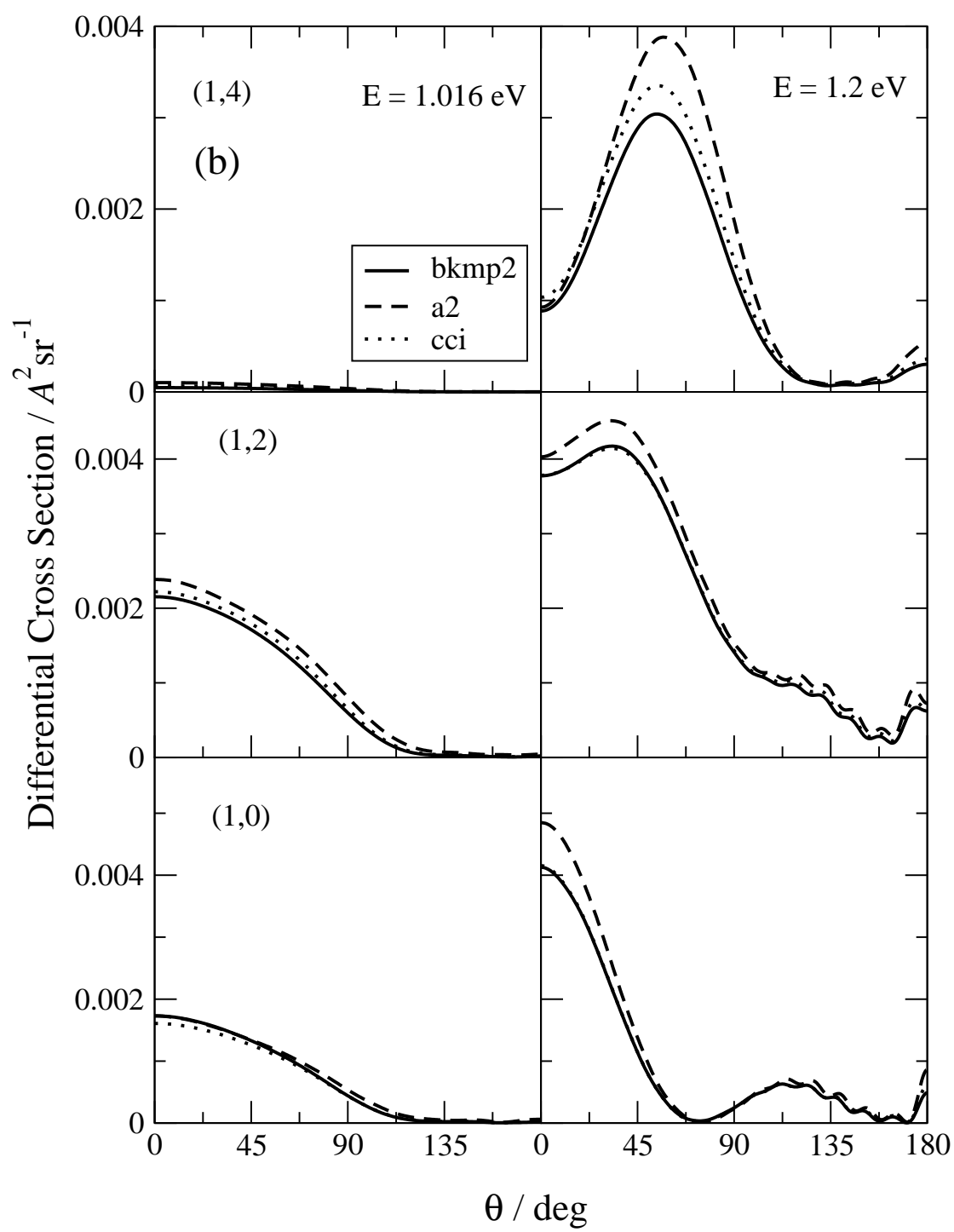


Figure 6(b)